DTIC COPY

AFRL-PR-ED-TR-2005-0068

AFRL-PR-ED-TR-2005-0068

An Investigation of Bremsstrahlung Reflection in a Dense Plasma Focus Device

Robert Thomas

AFRL/PRSP
10 E. Saturn Blvd.
Edwards AFB CA 93524-7680

March 2006

Special Report

APPROVED FOR PUBLIC RELEASE; DISTRIBUTION UNLIMITED.

AIR FORCE RESEARCH LABORATORY
AIR FORCE MATERIEL COMMAND
EDWARDS AIR FORCE BASE CA 93524-7048

UNCLASSIFIED

REPORT DOCUMENTATION PAGE	Form Approved OMB No. 0704-0188

1. REPORT DATE *(DD-MM-YYYY)*	2. REPORT TYPE	3. DATES COVERED *(From - To)*
12-09-2005	Special In-House Report	31 May 2005 – 19 Aug 2005

4. TITLE AND SUBTITLE **An Investigation of Bremsstrahlung Reflection in a Dense Plasma Focus Device**	**5a. CONTRACT NUMBER**
	5b. GRANT NUMBER
	5c. PROGRAM ELEMENT NUMBER 62500F
6. AUTHOR(S) Robert Thomas	**5d. PROJECT NUMBER** 48470159
	5e. TASK NUMBER
	5f. WORK UNIT NUMBER 549907
7. PERFORMING ORGANIZATION NAME(S) AND ADDRESS(ES) AFRL/PRSP 10 E. Saturn Blvd. Edwards AFB CA 93524-7680	**8. PERFORMING ORGANIZATION REPORT NO.**
9. SPONSORING / MONITORING AGENCY NAME(S) AND ADDRESS(ES) Air Force Research Laboratory (AFMC) AFRL/PRS 5 Pollux Drive Edwards AFB CA 93524-7048	**10. SPONSOR/MONITOR'S ACRONYM(S)** XC
	11. SPONSOR/MONITOR'S REPORT NUMBER(S) **AFRL-PR-ED-TR-2005-0068**

12. DISTRIBUTION / AVAILABILITY STATEMENT

Approved for public release; distribution unlimited. (DTIC Users Only). Public Affairs No. AFRL-ERS-PAS-2006-101.

13. SUPPLEMENTARY NOTES

14. ABSTRACT

An overview of Bremsstrahlung radiation, which is prevalent in high-temperature fusion plasmas, is given, as well as estimates for the power and energy flux to a reflector wall from a dense plasma focus device burning p-^{11}B. From these calculations, the wall temperature and ablation rate can be calculated. The physics derived from Inertial Confinement Fusion (ICF) Hohlraum use are applicable in the case where the wall temperature exceeds 10^5 K, and the reemission flux is estimated for various flux levels. Provided a method could be found for decreasing the incoming flux to the wall (low Z material shields, cooling methods), multilayer structures would provide the best method for reflecting soft and hard x-rays. Experimental results from high-energy photon experiments are provided.

15. SUBJECT TERMS

Fusion; plasma; physics; Bremsstrahlung; radiation; dense plasma focus; DPF; ablation; Hohlraum; multilayer; reflector

16. SECURITY CLASSIFICATION OF:			17. LIMITATION OF ABSTRACT	18. NUMBER OF PAGES	19a. NAME OF RESPONSIBLE PERSON
					Franklin B. Mead, Jr.
a. REPORT	b. ABSTRACT	c. THIS PAGE			19b. TELEPHONE NO *(include area code)*
Unclassified	**Unclassified**	**Unclassified**	A	54	(661) 275-5929

DTIC COPY

NOTICE

FOREWORD

This special report, entitled "An Investigation of Bremsstrahlung Reflection in a Dense Plasma Focus Device," presents the results of a research study performed under JON 48470159 by AFRL/PRSP, Edwards AFB CA. The Project Manager for the Air Force Research Laboratory was Dr. Franklin B. Mead, Jr.

This report has been reviewed and is approved for release and distribution in accordance with the distribution statement on the cover and on the SF Form 298.

/ signed /

FRANKLIN B. MEAD, JR.
Project Manager

/ signed /

RONALD E. CHANNELL
Chief, Propellants Branch

/ signed /

PHILIP A. KESSEL
Technical Advisor
Space & Missile Propulsion Division

This Page Intentionally Left Blank

TABLE OF CONTENTS

LIST OF FIGURES

LIST OF TABLES

GLOSSARY

A	Atomic Weight
C_f	Friction Factor
C_p	Specific Heat
D	Diameter
DPF	dense plasma focus
D-T	deuterium-tridium
E_{br}	Bremsstrahlung Energy
$erfc$	Complementary Error Function
e_t	Turbulence Parameter
d_{min}	Minimum Multilayer Thickness
g	Gaunt Factor
G	Free Stream Gas Flow
ΔH	Heat of Sublimation
h_o	Local Convective Coefficient
H_r	Recovery Enthalpy
H_w	Wall Enthalpy
H_v	Vapor Enthalpy
ICF	Inertial Confinement Fusion
k_t	Turbulence Correction Factor
kT_e	Electron Temperature
$k_{z1,2}$	Wave Vector Components
L	Length
ℓ_o	Scaling Constant
$\dot{m}_v$	Evaporation Rate
M	Atomic Mass Number
M_o	Scaling Constant
n	Number of Atoms
n	Refractive Index
n_e	Electron Density
n_i	Ion Density
N	Number Density
N	Reemission Factor

P	Pressure (Torr)
p-^{11}B	proton – Boron-11
P_{br}	Bremsstrahlung Power (W)
Pr	Prandtl Number
P_{tot}	Total Bremsstrahlung Power Density
q_c	Critical Momentum Transfer
$q_{cond,l}$	Liquid Conductive Flux
$q_{conv,g}$	Gas Convective Flux
$q_{rad,g}$	Gas Radiative Flux
Q_{tot}	Total Heat Flux
$\dot{Q}_{bo}$	Time Rage Change of Burnout Heat Flux
$\dot{Q}_{conv}$	Time Rage Change of Convective Heat Flux
$\dot{Q}_{rad}$	Time Rage Change of Radiative Heat Flux
Re	Reynolds Number
S_{hw}	Diffused Flux
S_i	Incident Flux
S_r	Reemitted Flux
S_s	Source Flux
St_o	Stanton Number
t	time (s)
t_w	Reflector Thickness (m)
T	Temperature
T_g	Gas Temperature (K)
T_r	Recovery Wall Temperature
T_{sat}	Saturation Temperature
T_w	Wall Temperature
U	Average Velocity (m/s)
x	Spatial Variable (m)
x_e	Corrective Spatial Variable (m)
$\bar{v}$	Mean Velocity (m/s)
V_{pin}	Pinch Volume (m^3)
Z	Atomic Number

Z_{eff}	Effective Atomic Number
$\tilde{\alpha}$	Evaporation Probability
α'	Scaling Constant
α	Thermal Diffusivity
β	Scaling Constant
δ	Film Thickness
Γ	Mass Flow Rate/Circumference
λ	Latent Heat of Vaporization
λ	Photon Wavelength
Ω	Empirical Correction Factor
κ	Thermal Conductivity
μ	Dynamic Viscosity
ρ	Density
ρ_g	Gas Density
ρ_l	Liquid Density
σ	Surface Tension
σ	Stephan-Boltzmann Constant
θ	Critical Angle
τ	Deposition Time
τ_p	Pinch Time
τ_w	Shear Stress
ν	Repetition Rate
ν	Scaling Constant
ξ	Static Property Parameter
ζ	Scaling Constant

This Page Intentionally Left Blank

1.0 EXECUTIVE SUMMARY

1.1 Abstract

An overview of Bremsstrahlung radiation, which is prevalent in high-temperature fusion plasmas, is given; as well as estimates for the power and energy flux to a reflector wall from a dense plasma focus device burning p-^{11}B. From these calculations, the wall temperature and ablation rate can be calculated. The physics derived from Inertial Confinement Fusion (ICF) Hohlraum use is applicable in the case where the wall temperature exceeds 10^5 K, and the reemission flux is estimated for various flux levels. Provided a method could be found for decreasing the incoming flux to the wall (low Z material shields, cooling methods), multilayer structures would provide the best method for reflecting soft and hard x-rays, and experimental results from high-energy photon experiments are provided.

1.2 Summary

An investigation of Bremsstrahlung radiation has been performed and it was seen that single film Hohlraum-like cavities are best suited due to the high energy flux levels. If the reflection cavity were made small enough for the flux levels to reach 10^{12} W/cm^2, the x-rays would be reemitted 10-12 times, according to numerical hydrodynamic models designed at Sandia National Laboratories. Multilayer structures provide a much greater range of energies over which photons can be deflected; however, they could not withstand the flux levels involved (~ 10^7 W/cm^2), have not been designed for the photon energies of interest (> 200 keV), and only reflect at very small angles of incidence (~ mrad). If these physics could be resolved, multilayer structures would provide an excellent option for the reflection of x-rays. Current tests are at the 100 keV energy range, with reflectivites close to 30%, which is lower than the 50% assumed in

the prior dense plasma focus (DPF) study. Further investigation of inverse-Bremsstrahlung is necessary to see if the 10 reemissions found in Hohlraums corresponds to at least 50% reflection.

1.3 Introduction

Bremsstrahlung radiation, which is German for “braking radiation,” occurs when charged particles are decelerated by collisions with other charged particles and emit photons. This form of radiation is pervasive in high temperature plasmas of fusion interest and constitutes an energy loss and cooling mechanism for the plasma. The problem of Bremsstrahlung emission is amplified in our case because of the high temperatures achieved by the p-^{11}B DPF pinch (~ MeV), and the radiation’s Z^2 dependence.

The purpose of this report is to investigate the reflection physics for the high-energy Bremsstrahlung radiation emission characterized in p-^{11}B DPF fusion. A literature search has been performed on Hohlraum cavities, multilayer reflectors, and several cooling techniques and will be presented. Fortunately, most of the numerical studies done at Sandia National Laboratory on Hohlraums are directly applicable to our case. The survey of the multilayer research shows that photon energy levels of DPF interest have not yet been investigated; however, the general trend is towards high energy reflection, and basic analytical models are produced. The vast majority of chamber cooling work that has been done concentrates on the transport mechanism of convection and ignores radiation. This obviously is not valid in our case; however, the basic analytical relations are offered to give insight into the areas needing to be investigated for successful cooling. Also, the mass flow rate is estimated which will give an idea of how much extra propellant needs to be carried. Finally, the results found here are compared to those assumed in the earlier DPF investigation burning p-^{11}B [1].

1.4 Bremsstrahlung Reflection

The issue of Bremsstrahlung reflection is critical for successful operation of the DPF device [1]. The underlying physics depend on the energy and flux of the incoming radiation to the wall. If the incoming angles and fluxes are small, then multilayer structures would provide the best option for reflection, since both hard and soft x-rays have been detected in experiments. If the fluxes and wall temperatures reach high enough levels (>10^5 K), then a plasma will be created at a wall, and numerical radiative hydrodynamic analysis is necessary to find the reemission of the photons. Both cases will be presented here, beginning with an estimation of the flux, temperature, and ablation at the wall using classical heat transfer relations.

1.5 Bremsstrahlung Radiation

In order to correctly ascertain the relevant reflection physics, it is first necessary to define the incoming energy and power flux to the wall. The Bremsstrahlung emission spectrum is given by [2]:

$$\frac{dP_{br}}{d\lambda} = 6.01\times10^{-36}\,\frac{g n_e^2 Z_{eff}}{\lambda^2\sqrt{kT_e}}\exp\left(\frac{-12.40}{\lambda kT_e}\right), \tag{1}$$

where λ is the photon wavelength, n_e is the electron temperature, Z_{eff} is the effective atomic number, and kT_e is the electron temperature. The “Gaunt factor” g, which takes into account quantum effects, approaches $2\pi^{-1}(3)^{1/2}$ at high plasma temperature (> 550,000 K) [3]; and this value is used in the analysis. The peak Bremsstrahlung emission wavelength (angstroms) is

$$\lambda_{\max} = \frac{6200}{kT_e\,(\text{eV})} \tag{2}$$

The total Bremsstrahlung power density is estimated using [2]:

$$P_{tot} = 5.35 \times 10^{-37} Z_{eff} n_e^2 (kT_e)^2 , \tag{3}$$

where Z_{eff} is defined as:

$$Z_{eff} = \frac{1}{n_e} \sum n_i Z_i^2 \tag{4}$$

and has a value of 13 for the p-^{11}B reaction. The electron density is on the order of 10^{25} m^{-3}, and the ion temperature 1.5 MeV, which gives a Bremsstrahlung power density of 5 x 10^{15} W/cm^3. The wall loading (input flux) is set equal to the Bremsstrahlung output power divided by the area of the wall that is exposed to the plasma. The radiation energy after each pulse is found by:

$$E_{br} = \tau_p P_{tot} V_{pin} \tag{5}$$

where τ_p is the pinch lifetime, and V_{pin} is the volume of the pinch region of the DPF device. The power deposited to the wall is found by multiplying the energy with the repetition rate ν:

$$P_{br} = E_{br} \nu \tag{6}$$

Using the values found from the DPF study [1] for a 500 kN propulsion unit, an energy and power flux of 1.23 x 10^5 J/cm^2 and 1.26 x 10^6 W/cm^2 are found, respectively. These values will be used for the rest of the report.

1.6 Wall Heating and Evaporation

In this section the evaporation rate and wall temperature will be estimated using classical heat transfer. Once an estimation of these parameters is found, a more accurate analysis can be obtained. The analysis will closely follow the work done by Kammash [4], who formulated the problem under conditions of thermonuclear interest. When a solid is heated to a high temperature, some of the atoms that are in the high-energy tail of the thermal distribution will have sufficient energy to overcome the surface binding energy; if the momentum of these atoms at the surface is directed away from the surface, they will evaporate. The rate of evaporation can be estimated from the vapor pressure of the solid material above the surface and is given by [4]:

$$\frac{dn}{dt} = \tilde{\alpha}\frac{N\bar{v}}{4}, \tag{7}$$

where $\tilde{\alpha}$ is the probability that an atom from the gas phase sticks at the surface (generally set equal to 1), and $\bar{v}$ is the mean velocity. Noting that $P = NkT$, and that the mean velocity is proportional to $(T/M)^{1/2}$, Equation (7) can be put in the form

$$\frac{dn}{dt} = \frac{3.5\times10^{22}}{\sqrt{M}}\frac{P(T)\,[\mathrm{Torr}]}{\sqrt{T}\ (\mathrm{K})}, \tag{8}$$

where M is the atomic mass number. The most severe thermal loading on the wall occurs when the plasma is at the end of a discharge and the plasma is "dumped" on the wall in a very short period of time. In order to calculate the number of atoms evaporated during one heat pulse, we must first calculate the temperature increase in the solid as a result of sudden heating. This temperature will also be used to find the amount of cooling necessary. An outline and solution of the problem is given, and the reader is referred to Kammash [4] for the complete analysis.

The equation of interest in this case is the unsteady heat conduction equation which is applied to a semi-infinite solid so that the temperature is a function of one spatial dimension only (neglects curvature); i.e.,

$$\frac{\partial^2 T}{\partial x^2} = \frac{1}{\alpha}\frac{\partial T}{\partial t}, \qquad (9)$$

where

$$\alpha = \frac{k}{\rho C_p} \qquad (10)$$

is the thermal diffusivity, k the thermal conductivity, C_p is the specific heat at constant pressure, and ρ is the density of the solid. An illustration of 1-D heat conduction and the associated boundary conditions are shown in Figure 1.

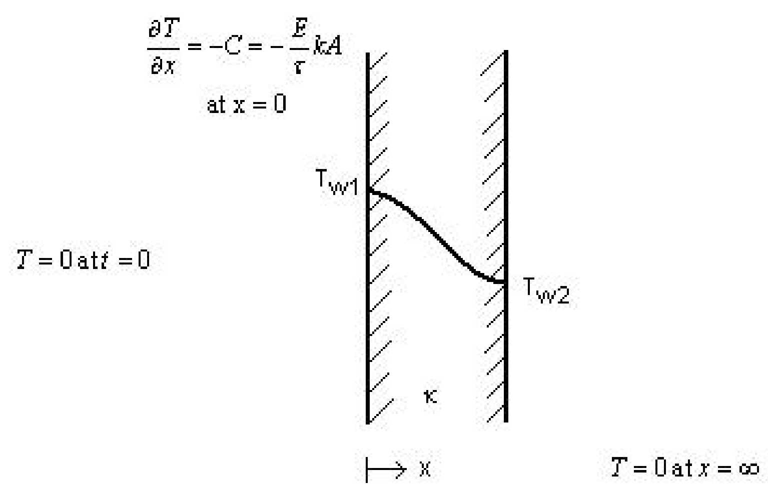

Figure 1: 1-D Heat Conduction Illustration

The boundary conditions are:

$$T = 0 \text{ at } t = 0$$

$$\frac{\partial T}{\partial x} = -C = -\frac{E}{\tau} kA \text{ at x} = 0 \tag{11}$$

$$T = 0 \text{ at } x = \infty$$

The second boundary condition represents the heat flow into the solid whereby a total energy E_{br} is dumped in the area *A* in the time τ. The complete solution of Equation (9) during the heating phase (t < τ) can be written as

$$T(x,t) = C\sqrt{\alpha}\left[2\sqrt{\left(\frac{t}{\pi}\right)}\exp\left(\frac{-x^2}{4\alpha t}\right) - \frac{x}{\sqrt{\alpha}}\operatorname{erfc}\left(\frac{x}{2\sqrt{\alpha t}}\right)\right], \tag{12}$$

where the function *erfc(x)* is related to the familiar error function erf(x), by

$$erfc(x) + erf(x) = erf(\infty) = 1 \tag{13}$$

At the surface (x = 0), Equation (12) reduces to

$$T(0,t) = \frac{E}{A\tau}\sqrt{\frac{4}{\pi\rho k C_p}}\sqrt{t} \tag{14}$$

The maximum temperature occurs at $t = \tau$, which is due to the dumping of energy per unit area in time τ:

$$T(0,\tau) = (\Delta T)_{\max} = \frac{E}{A}\frac{1}{\sqrt{\tau}}\sqrt{\frac{4}{\pi\rho k C_P}} \tag{15}$$

This temperature increase is of interest because it is indicative of the other reflection physics at the wall. Also of special interest is the surface temperature shortly after the end of heating, which can be approximated as

$$T(0,t) = T_{\max} \exp\left(-\sqrt{\frac{t}{\tau}} \right) \tag{16}$$

To find the number of atoms evaporated during each heat pulse, it is necessary to assume uniform deposition during the dumping time τ, constant heat of sublimation ΔH, constant thermal conductivity k, and a constant specific heat C_p in the temperature range of interest. The number of atoms evaporated during each pulse is obtained by substituting Equation (7) along with Equation (8) into Equation (12) and integrating over the heating period. The corresponding number during the cooling phase is obtained using a similar process. The end result is

$$n = 0.2\tau \frac{dn}{dt}(T_{\max}), \tag{17}$$

where the dn/dt term is the time rate change in atoms evaluated at T_{max}. This equation is used to find the thickness of ablated material per pulse, which is shown in Figure 2. The number of pulses goes up to roughly 8.5 x 10^5 pulses, which is how many times it would fire if it ran at a repetition rate of 10 Hz continuously for one day.

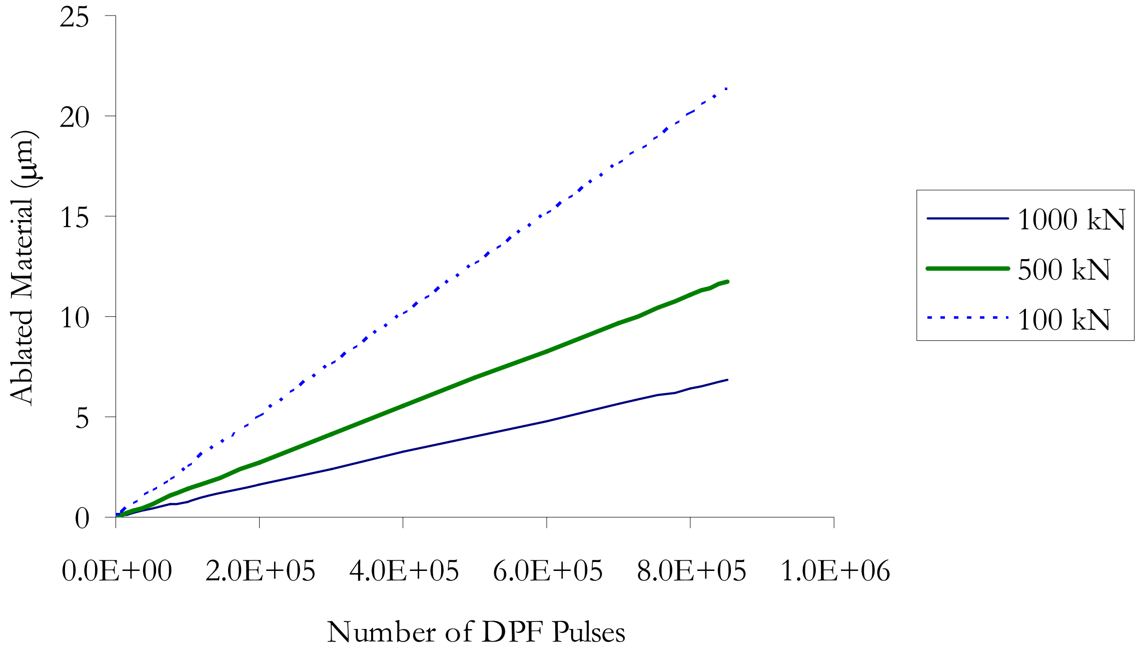

Figure 2: Ablated Material as a Function of DPF Pulses

Also of interest is the wall temperature as a function of wall "dumping" time, which is shown in Figure 3.

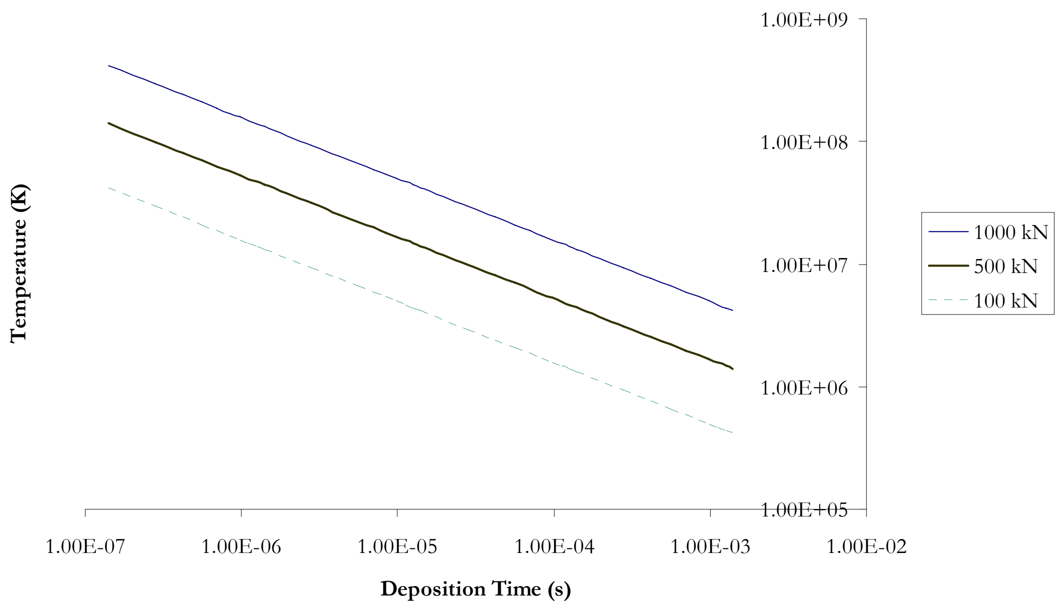

Figure 3: Log Scale of Deposition Time vs. Temperature

It can be seen that the temperatures reach above 10^5 K, and when the temperature of the wall begins to exceed this value, the wall will itself become an intense radiator and eventually determine the radiation field in the cavity. The requisite physics have been studied in the use of Hohlraums, which is discussed in the following chapter.

2.0 X-RAY CONFINEMENT PHYSICS

2.1 Hohlraum Cavities

The investigation of x-ray confinement in fusion systems has been driven by research on the use of Hohlraums in Inertial Confinement Fusion (ICF). In ICF, small, spherical fuel pellets are imploded by high-power lasers or ion beams. In order to achieve symmetric compression, the pellets can be placed in cylindrical gold-plated cavities called Hohlraums. The Hohlraum contains small holes through which beams pass, and when targeted by a laser or ions, the Hohlraum converts the beam into soft x-rays on the inner wall, which subsequently provide indirect heating of the total inner wall. The confinement effect arises because the cavity wall heats up due to the heating from this source and becomes itself a strong emitter of thermal soft x-ray radiation [5]. In this way a fraction of the flux which the wall receives from the source is reemitted from the cavity. A diagram of the ICF concept utilizing a Hohlraum is illustrated in Figure 4 [6].

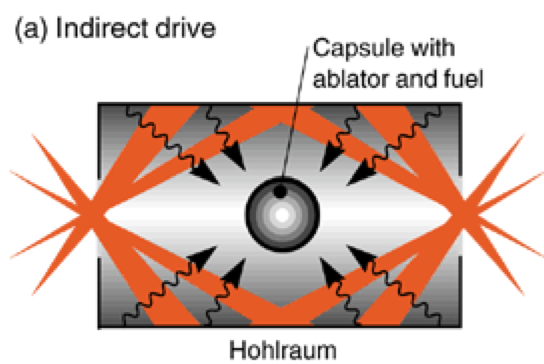

Figure 4: Indirect Drive ICF Concept

Thus far, ignition experiments have used indirect drives in which an external laser light heats the Hohlraum cavity. The light is converted with close to 100 percent efficiency into an intense flux of x-rays of almost 1,000 terawatts per square centimeter [6]. The x-rays converge on the capsule's outer ablator layer, heating and expanding it. The rocket-like blow-off of the ablator then pushes the rest of the capsule inward, compressing the interior fuel to extreme pressures and temperatures.

2.2 Numerical Models

Quantitative modeling of the injection of several laser beams into the cavity, the subsequent conversion of the laser light into soft x-rays, and the resulting spatial distribution of energy deposition possess considerable difficulties, owing to the complicated geometry and the rather involved physics of laser light conversion [5]. In order to reach a more tractable model, the laser is replaced by a fictitious source of x-rays located inside the cavity wall. In our case, this x-ray source is the Bremsstrahlung radiation produced from the DPF device, and the pinch region will serve as the target region as opposed to a frozen D-T pellet.

In the physics model it is also assumed that radiation and matter are in complete thermodynamic equilibrium in the cavity; i.e., the wall emits Planck radiation according to Boltzmann's equation into the cavity, and the loss of energy by diffusion into the wall can be calculated by an approximation of radiation heat conduction. The reemission of the x-rays is determined by a nonlinear heat wave which forms on the inside of the wall. A diagram of the wave propagation process is illustrated in Figure 5 [7]. At time $t = 0$ (a) the body is brought into contact with a thermal bath. For $t > 0$ (b) first a nonlinear heat wave runs into the undisturbed material. Subsequently, hydrodynamic motion of the heated material becomes important; and the heat wave is overtaken by a shock wave and the ablative heat wave forms.

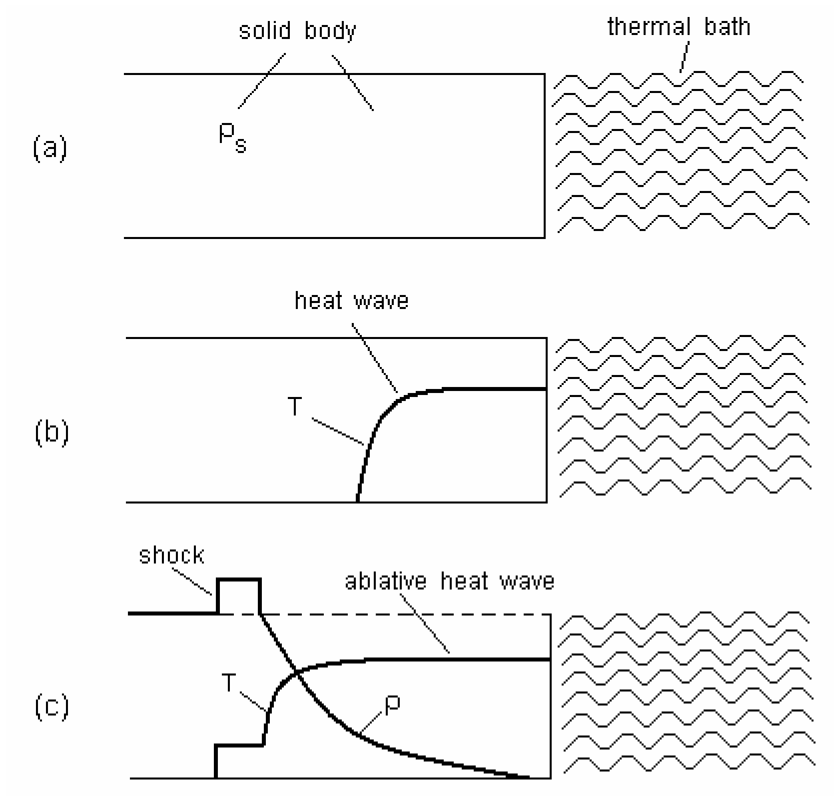

Figure 5: Heating of a Solid Body in Contact with a Thermal Bath

Additionally, cases have been studied of a cavity with (open) and without (closed) holes [6]; the latter being where our interest lies, since we won't encounter external laser heating.

2.2.1 Similarity Analytical Model

There have been varying levels of sophistication in the x-ray reflection models produced, but in general, the following is true. The key parameter for describing radiation confinement in a cavity is the *reemission coefficient* of the x-ray heated wall [5]. It is determined by a radiation-driven ablative heat wave propagating into the depth of the wall material, as described by Pakula and Sigel [7]. To understand the situation, consider the case where a solid gold wall is irradiated from the left with a constant radiation flux, as shown in Figure 6.

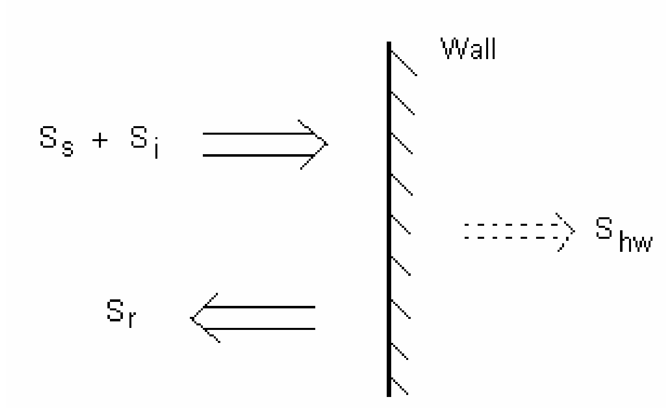

Figure 6: Flux at the Interface Between Wall and Inner Cavity

The wall receives a flux S_s from a source and an incident flux S_i of thermal radiation from the other wall elements in the cavity. The wall radiates a reemitted flux S_r into the cavity, whereas a net heat flux S_{hw} of radiation diffuses into the wall by a process known as photon diffusion. The energy balance of this process is given by:

$$S_s + S_i = S_r + S_{hw} \tag{18}$$

For a completely closed cavity (no holes), the source flux must flow into the wall; there is no other loss than the heat propagation into the wall. In this case, the temperature at the boundary between the ablation heat wave and the vacuum is given by the self similar solutions for the ablative heat wave in gold as [5]:

$$T = 3.11 \times 10^6 S_s^{4/13} t^{2/13} \quad \text{(K)} \tag{19}$$

where the units of flux are in 10^{14} W/cm^2 and the units of time in nanoseconds. A plot of the wall temperature in the time frame of interest is shown in Figure 7.

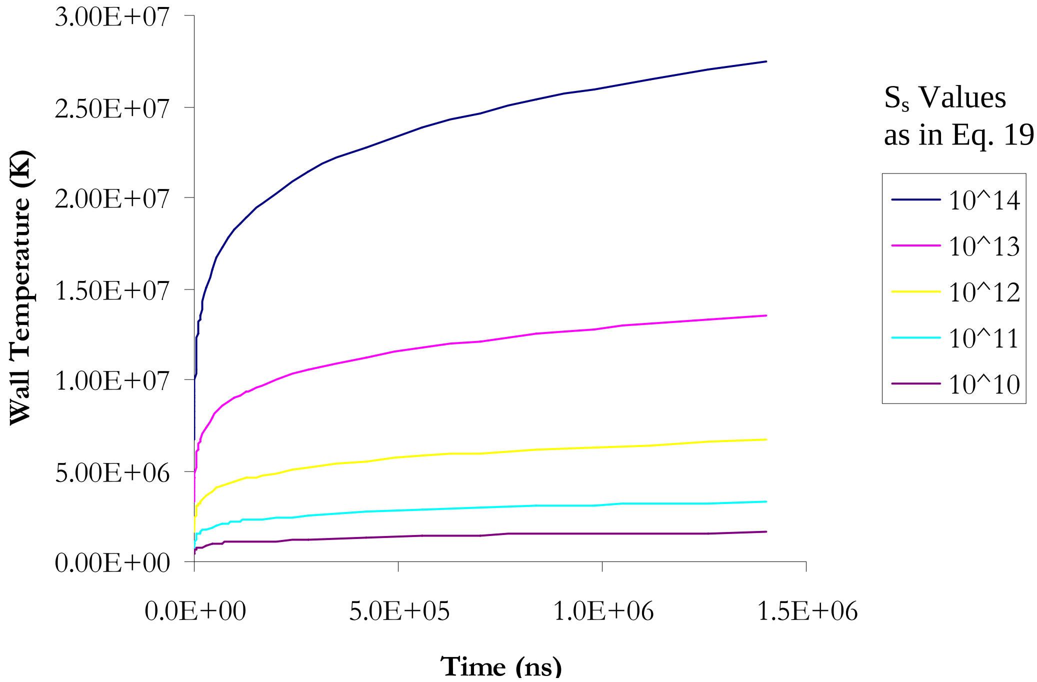

Figure 7: Wall Temperature as a Function of Heating Time

For blackbody radiation, the reemitted flux S_r has the form:

$$S_r = \sigma T^4 \tag{20}$$

Therefore, the reflected flux and temperature can be obtained from the source flux and time. The ratio $N = S_r / S_{hw}$ is called the reemission factor of the wall and is a measure for the quality of radiation confinement. The factor N characterizes the wall and depends on the material as well as time. Physically it corresponds to the number of reemissions of the source energy inside the cavity. A plot of the reemission coefficient with the input Bremsstrahlung flux as a parameter is shown in Figure 8.

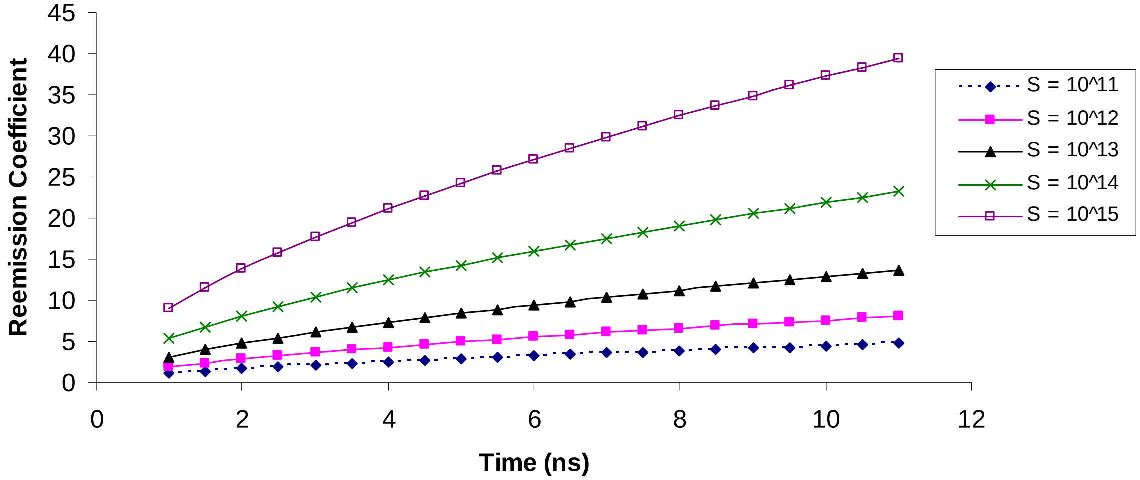

Figure 8: Reemission Coefficient vs. Time for Various Bremsstrahlung Fluxes on Gold (Similarity Model)

It should be noted from this plot that the number of reemissions increases strongly with absorbed radiation flux and time. A more complete model that takes into account the atomic structure and material opacity is described below.

2.2.2 Murakami Computational Model

More advanced models have been used to estimate the reemitted x-ray flux. Again using an ablative heat wave to model the x-ray flux inside the reflector, Murakami [8] assumed the coefficient for radiation thermal conductivity is directly related to the radiation mean free path and, therefore, to the Rosseland mean opacity. Taking the power law approximation for the frequency averaged mean free path (Rosseland mean):

$$\ell = \frac{\ell_o T^{\alpha'}}{\rho^{\beta}} \tag{21}$$

With temperature T, density ρ, and parameters ℓ_o, α’, β, Murakami obtains the scaling law for the reemitted flux in the form:

$$S_r = M_o S_a^{\upsilon} t^{\varsigma} \tag{22}$$

where S_a is the absorbed flux and is set equal to the energy flux calculated in Equation 5, and t is time. The constants M_o, ν, ζ, and time t, can be analytically derived by first adjusting (21) to corresponding opacity properties, and then determining the reemitted flux in (22) by using the analytic relations given in Reference 9. A best fit of these scaling laws to actual numerical simulations that take into account the full complexity of the equation of state and opacity tables in the appropriate temperature and density regions has been tabulated [7]. For gold, Equation (22) becomes:

$$S_r = 13.0 S_a^{1.05} t^{0.46}, \tag{23}$$

where the fluxes are in units of 10^{14} W/cm^2 and time is in the units of 10^{-8} s. An important result not shown here from Murakami's analysis is that high Z gold reemits incident radiation ten times more efficiently than low Z-carbon; and vice versa, carbon absorbs ten times more per unit area than gold when in contact with the same radiation field. By using (23), a plot of the reemission coefficient vs. time can be reproduced.

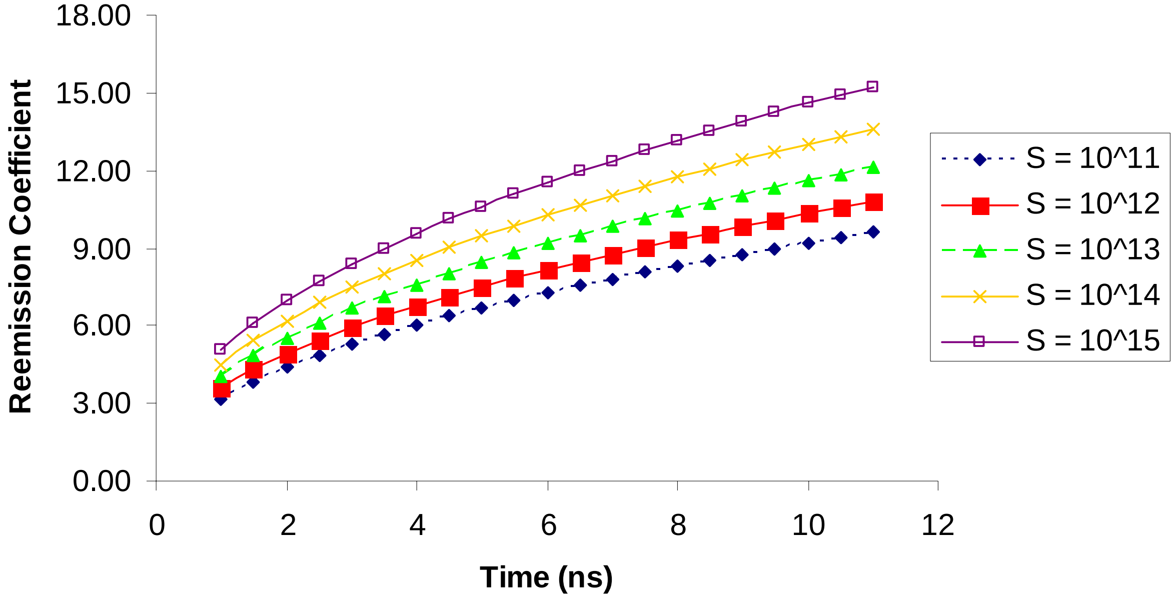

Figure 9: Reemission Coefficient vs. Time for Various Bremsstrahlung Fluxes For Gold (Murakami Model)

The flux and time values in this figure are the same as in Figure 8. The immediate difference that can be seen from Figures 8 and 9 is that the reemission coefficient N depends very weakly on the absorbed flux and on time approximately at $t^{1/2}$. This gives N values a factor of 2-3 times smaller than the Similarity Model. Experiments have shown that the scaling laws described by Murakami are in better agreement with x-ray confinement tests performed in the laboratory, although improved opacity calculations are desired [8]. Another trend that is evident is that the reemission coefficient increases with incoming flux, which would suggest a smaller surface area reflector would be desirable. For instance, in the case of absorbed flux of 10^{13} W/cm^2, the x-rays would be reemitted roughly ten times before being lost.

There are certain limitations to using a Hohlraum-like cavity. The design and analysis assume a constant input flux and radiation spectrum, which will not be the case during the collapse of the pinch. Furthermore, it can be seen from both models that the reemission coefficient increases with the incoming wall flux, which would suggest the use of small confinement cavities. Although the ablation material depth is typically on the order of microns, for longer missions (months – years) this can add up over hundreds of thousands of pulses spanning over an extended operating period. Cooling of the Hohlraum material would only decrease its performance, as it would decrease the plasma intensity inside the wall and limit the number of reemissions. Because of these shortcomings, the use of multilayer materials needs to be investigated, as well as the cooling techniques necessary for their proper use. Additionally, a simple analytical analysis will show that multilayer structures have superior reflectivities than those of gold alone.

3.0 MULTILAYER REFLECTORS

3.1 Introduction

Broad-band optics for x-rays have traditionally consisted of high Z, high density, single element thin-films (e.g., gold), reflecting in grazing incidence by total reflection [10]. A promising alternative is the "super-mirror multilayer structure," in which the layer spacing has been gradually decreased as a function of depth. Lead, Tungsten, and numerous carbides are the materials that are have been tested for these structures. The lower energy z-rays will be totally reflected from the surface layer, while the harder x-rays will penetrate into the multilayer until a region is reached where the layer spacing is such that the x-ray is reflected. The principle is schematically illustrated below [10].

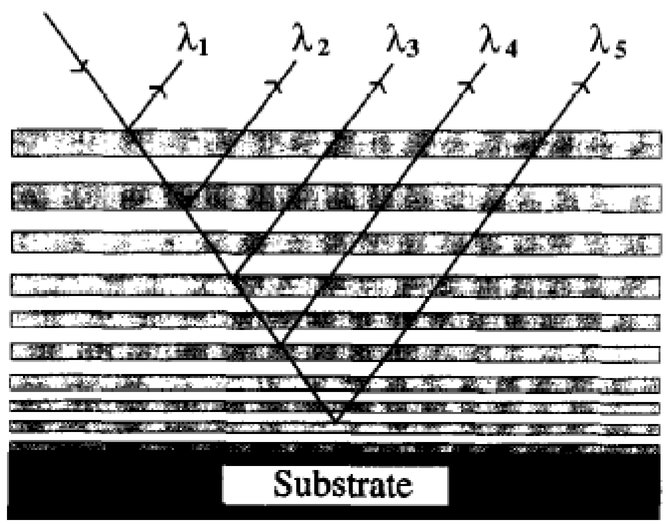

Figure 10. Principle of Broad Band X-ray Reflection

Depth-graded x-ray multilayers consist of bilayers comprising material pairs selected for both their optical and material properties, with a range of bilayer thicknesses chosen so as to reflect over a wide energy band; multilayers designed for use above 100 keV in particular contain hundreds to thousands of nanometer-scale layers having near perfect interfaces in order to achieve optimal performance [11].

3.2 Reflector Theory

Multilayer structures work on the principle of total reflection, which is illustrated in Figure 11 [12]:

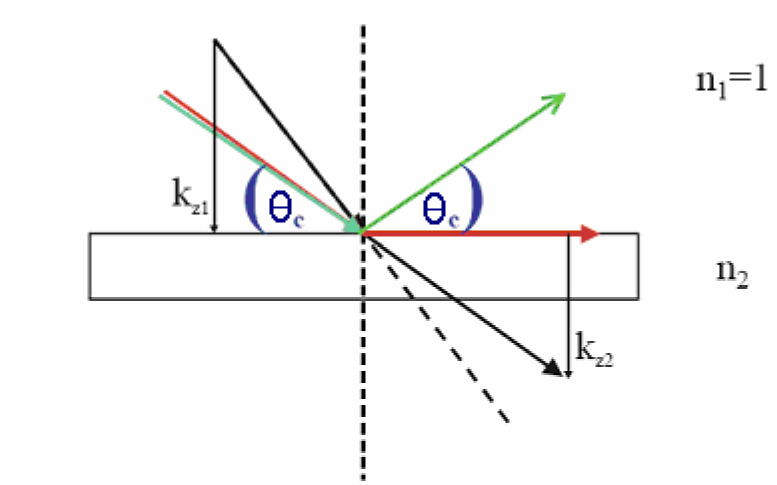

Figure 11: The Principle of Total Reflection

The reflective index *n* is a ratio of the corresponding perpendicular wave vector components k_{z2} and k_{z1} when a photon passes an interface between vacuum and matter. Consider a photon traveling within a vacuum ($n_1 = 1$) with the sample material having a refractive index n_2. In case n_1 is larger than n_2, the photons will be refracted away from the normal direction (black arrow). Inside the material, the perpendicular component of the photon vector is reduced to k_{z2} compared to its value k_{z1} outside the material. As the angle of the incident photon becomes smaller, a so-called evanescent wave traveling along the surface is created (red arrow). A further decrease of the angle of incidence leads to total reflection. The incoming radiation practically cannot penetrate the material (green arrow). The angle of incidence, at which total reflection occurs, is called the critical angle θ_c.

Total reflection is limited to a regime in which the reflected photon momentum transfers q is less than the critical momentum transfer (below which total reflection occurs) [10]:

$$q_c = 0.0292\left(\frac{\rho Z}{A}\right)^{1/2}, \tag{24}$$

where Z is the atomic number, A is the atomic weight, ρ is the density (g/cm^3) and units of q_c are in Å^{-1}. The corresponding critical angles and energies can be found by noting that for specularly reflected x-rays, the momentum transfer is

$$q = \frac{4\pi \sin\theta}{\lambda} \tag{25}$$

And the energy of incoming x-ray (keV) is given as a function of the wavelength (angstroms) by:

$$E = \frac{12.398}{\lambda} \approx \frac{4\pi}{\lambda} \tag{26}$$

By combining (25) and (26) one obtains $q = E \sin \theta$. This implies that high photon energy applications require reflection at very small angles, which in turn requires very long mirrors with very stringent figure criteria. A gold mirror reflecting up to 80 keV would thus require a 1 mrad angle of incidence and a length of 1 m to reflect a 1 mm wide beam.

Due to interface effect and the proximity of different materials, multilayer structures have unique properties different from single film materials [13]. Depth graded x-ray multilayers consist of bilayers comprising material pairs (i.e., W/SiC) selected for both their optical and material properties, with a range of bilayer thicknesses chosen so as to reflect over a wide energy band. The peak reflectance attainable from an x-ray multilayer depends in practice on the reflection coefficient (ratio of reflected/scattered power to incident power) at each interface, determined by the optical constants (e.g., opacity) of the materials and by the interface width that characterizes the degree of interface perfection [12]. The energy of the hardest x-ray that may be reflected by the structure can be found by utilizing Bragg's Law:

$$\lambda = 2d_{\min} \sin\theta \tag{27}$$

in which d_{min} is the thickness of the bottom layer. By combining this with the relation given by (26) we are able to obtain

$$\frac{6.199}{d_{\min}} = E \sin\theta \approx q \tag{28}$$

This value of q is almost four times higher than the value of a gold film reflector. The reflection band of an optimal supermirror may therefore be expected to be a factor of 4 wider than the band of a thin-film reflector. However, this additional bandwidth is gained at the cost of reflectivity; absorption reduces the reflectivity at energies where reflection happens within the supermirror. The added bandwidth outweighs the lost reflectivity in the case of Bremsstrahlung radiation, since both soft and hard x-rays are present.

3.3 Experimental Findings

To illustrate the advantages of multilayers over single film reflectors, a comparison has been done measuring the 20 – 95 reflectivity of an Au-coated reflector and a 600 element bi-layer W/Si supermirror. The results of the study are shown in Figure 12 [10].

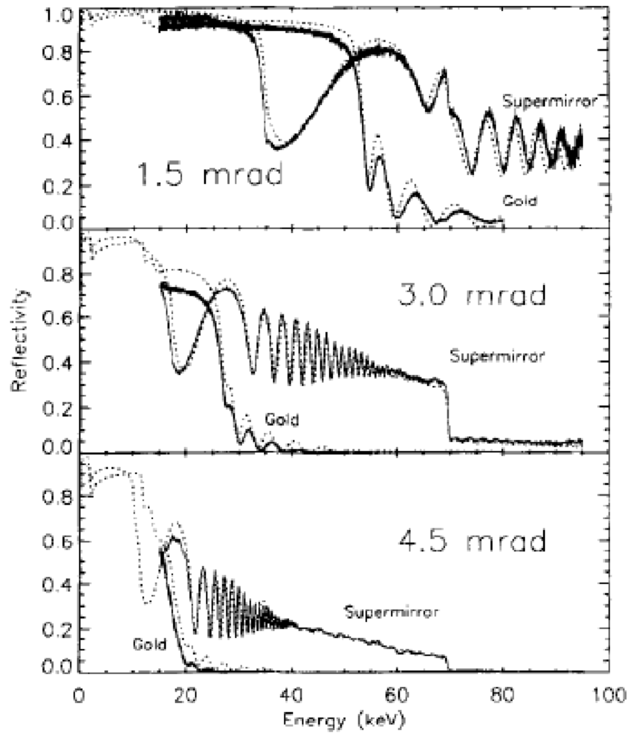

Figure 12: Comparison of Reflectivities of W/Si Supermirror and Gold Film

In comparing the measured reflectivities of the supermirror and the gold coating, the ability of the supermirror to reflect at higher energies is clearly seen. For angles of 4.5 and 3.0 mrad, the cutoff of the W/Si multilayer is determined by the absorption at 69.5 keV. At 1.5 mrad, the absorption edge is seen to have little effect, and one may therefore expect considerable reflectivity (~ 200 keV) at this angle. The major limitation of the supermirror, i.e., a reflectivity far from unity, is also clearly illustrated by the measurements. This is especially severe for the higher angles, but at 2 mrad and below, a reflectivity above 30% is obtained in the whole band. In order to overcome this problem, other material combinations could be used in the mirror, and are being investigated. Using Equation (2), it is seen that the highest energy photons will be coming in with an energy of over 200 keV, which is above the limits currently known. However, W/ SiC supermirrors have already been produced [12] and have been shown to reflect well above

100 keV. Also, if the bulk of x-rays are going to be in a narrow bandwith, a multilayer could be fabricated with a larger reflectivity in this band of interest.

Although the added bandwith would be a major advantage over single film reflectors, there are several shortcomings. The first problem is that the incoming flux from the DPF pinch would quickly destroy the multilayer. A combination of cooling methods (e.g., regenerative and film) might aid in solving this problem and are discussed in the next chapter. However, it is likely that additional approaches may be necessary, such as shield absorber made of ceramics or other low Z material. Also the photon energies of interest (> 200 keV) have not yet been examined. The final major concern is the small angles (~ mrad) necessary for reflection. This consideration would make a reflector much larger than the pinch region unnecessary, since any radiation coming in at a large angle would not be reflected. If these obstacles can be overcome, then the multilayer would provide an attractive alternative to single film layers. The reflectivity of 30% obtained in current experiments is lower than the 50% assumed in the original DPF report [1]; however, the advances cited may increase this number in future experiments.

4.0 WALL COOLING METHODS

4.1 Introduction

The current literature on multilayer structures deals with flux rates much lower that those expected with typical DPF operation. At the flux level and wall temperatures involved, the multilayer would be quickly destroyed; therefore, an active cooling system will be necessary. Much of the work that has been done in this area relates to the cooling requirements of combustion chambers in chemical rockets. Concepts developed to cope with this problem, either singly or in combination, include regenerative cooling, radiation cooling, film or transpiration cooling, ablation, and inert or endothermic heat sinks [14]. For the temperatures encountered with the DPF device, it will be necessary to use a combination of regenerative cooling and liquid film cooling. Many liquid rocket engines employ a film of liquid fuel as thermal protection for the combustion walls.

4.2 Film Cooling

The liquid film cooling process was experimentally studied in the 1950's and 1960's; however, no general theoretical model was ever developed. The classical approach of solving liquid film cooling problems is a turbulent flat plate correlation using either Reynolds's Analogy, which assumes identical velocity and temperature profiles in the laminar vapor sublayer, or Colburn's equation based on the 1/7th power law to characterize the velocity profile [15]. However, the formulation of this problem is difficult to obtain because of the complex phenomena that characterize the flow of a high velocity gas over a liquid film. Additionally, most of the investigations have been characterized by ambient pressure and temperature, essentially zero heat transfer rates, and relatively low interfacial shear forces. Such conditions are significantly different from those that characterize the typical application of liquid-film cooling, especially at the DPF conditions considered here. Also, radiative transfer, which is prevalent in our case, is not for most chemical rocket chambers; and therefore has received very little attention. Due to the lack of experimental and theoretical data in our operating regime, only the basic relations will be presented to give an order of magnitude estimate for the cooling requirements.

In liquid cooled systems, fundamental problems include the coolant mass flow rate required to cool the desired internal surface area, the intact liquid film length, and the effect of the cooling process on the performance of the engine [16]. The basic analytical and design problem can be stated as that of determining, for given liquid and gas flow parameters, 1) the rate of coolant injection required to establish a desired wetted area; and 2) the degree of the insulating effect of the gas-vapor layer downstream of the liquid film. The primary objectives of a liquid film cooling model are to predict the temperature profile along the chamber wall and to determine the film-cooled length to ensure that sufficient liquid film is injected across the reflector. By looking at the mass transfer properties, the necessary mass flow rate can be estimated.

4.2.1 Mass Transfer

The mechanisms involved in liquid film cooling are depicted in Figure 13 [15]. Heat is transferred from the hot free-stream gas to the liquid film by both radiation and convection. Heat energy from the hot gas stream increases the sensible enthalpy of the liquid by radiation, convection and conduction. After the saturation temperature of the liquid film is reached, the incident heat is used to vaporize the coolant. The liquid film terminates at some point downstream of the injector as a result of evaporation and its entrainment into the core gas stream.

The distance from the injector to the termination point is the liquid film-cooled length. Downstream of the liquid termination point, the vapor provides thermal blockage through gaseous film cooling.

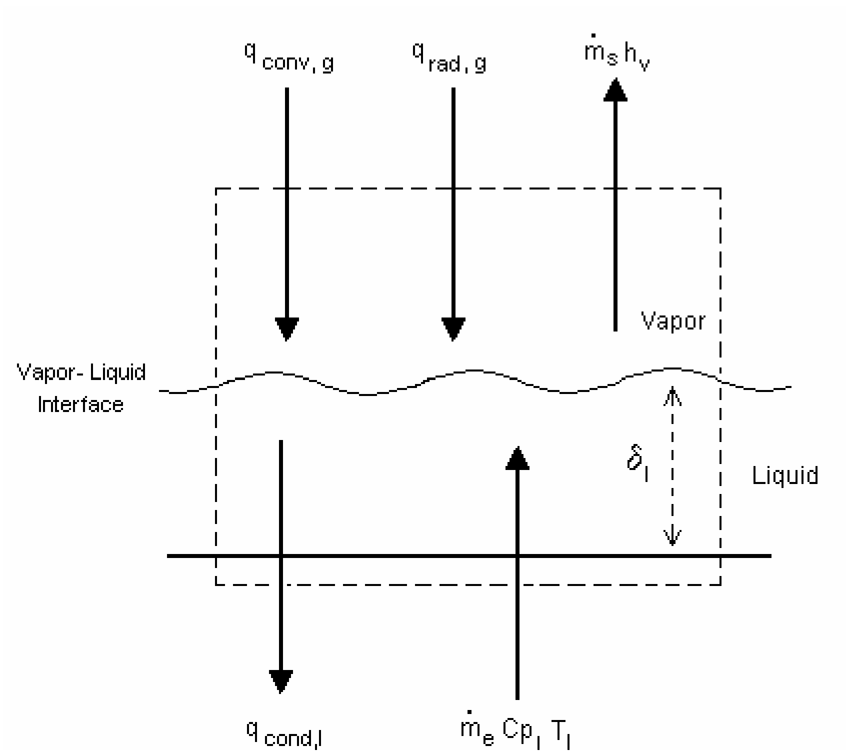

Figure 13. Control Volume for Interfacial Energy Balance

This energy is absorbed by vaporizing the liquid in the protective film on the wall. The vapor-generated flow is known as the transpiration cooling process. Downstream of the liquid film, the vapor mixes with the free stream gas entrained in the boundary layer, lowering the wall temperature through the well-known "gaseous film cooling" process. This provides thermal protection downstream of the dryout point.

The total heat flux due to both convection and radiation, Q_{tot}, is absorbed in the liquid film, causing an initial temperature rise [17]:

$$\frac{dT_{liq}}{dx} = \frac{Q_{tot}}{\Gamma C_p} \tag{29}$$

where Γ is the local liquid mass flow rate per circumference. After the liquid film reaches the saturation temperature T_v, the evaporation rate is:

$$\dot{m}_v = \frac{\dot{Q}_{tot}}{\lambda} = \frac{\dot{Q}_{conv} + \dot{Q}_{rad}}{\lambda} \tag{30}$$

where λ is the latent heat of evaporation. In most rocket combustion chambers, the radiant heat flux is negligible in comparison to the convective heat flux [17]. However, this will be the complete opposite for typical DPF operation, and the radiant heat flux will largely determine the evaporation rate as shown in Equation (2). The radiant heat flux can be estimated through the use of Equation (6) divided by the surface area of the exposed wall.

$$\dot{Q}_{rad} = P_{Br} / Area \sim 10^7 \text{ W/cm}^2 \tag{31}$$

This flux level is well above levels found in chemical rockets. Because of this tremendously high flux, another concern is that some of the radiant heat can penetrate the liquid film and be absorbed directly at the combustion chamber walls. With high enough heat flux, the liquid film can "burnout," as in normal pool boiling. Monde and Katto [18] have studied this problem for heat fluxes on the order of 10^6 W/m^2 and have correlated the burnout heat flux as:

$$\frac{\dot{Q}_{bo}}{\rho_v \lambda U} = 0.0591 \left(\frac{\rho_l}{\rho_v}\right)^{0.725} \left(\frac{\sigma}{\rho_l L U^2}\right)^{0.333} , \tag{32}$$

where ρ_v, and ρ_l are the densities of the vapor and liquid, σ is the surface tension, λ is the latent heat of vaporization, L is the length of the heated surface, and U is the average velocity of the liquid film. It has been realized experimentally that when the critical heat flux is exceeded, the liquid film separates from the heated surface. However, it is possible that this separation from the surface in the experiments may have been due to the constant heat flux condition imposed. In DPF operation the liquid film may be less susceptible to burnout than those in the heat transfer experiments, because separation of the liquid film from the surface would generate a region of droplets and bubbles which would cause scattering, decreasing the radiative transmission through the film. Use of these burnout correlations is questionable, since they are expressed in terms of the overall heated length. Ideally, the burnout point should be expressed in terms of local conditions, such as the local film thickness. This is why this analysis is mainly useful as an order of magnitude calculation.

The convective heat flux can be estimated using [17]:

$$\dot{Q}_{conv} = h_o \Delta T \,, \tag{33}$$

where h_o is the local convective coefficient and can be calculated from:

$$h_o = K_t G C_{pg} St_o \,, \tag{34}$$

where K_t is the turbulence correction factor given by:

$$K_t = 1 + 4e_t \tag{35}$$

The parameter e_t has a value of 0.05 – 0.2 depending on the turbulence intensities and distances from the liquid film injector, and we will use a value of 0.1. St_o is the Stanton number defined as:

$$St_o = \tfrac{1}{2} C_f \, \mathrm{Pr}^{-0.6} \tag{36}$$

The Stanton number is a dimensionless parameter typically made up of other, more familiar dimensionless parameters. It can be defined for heat transfer or for mass transfer. C_f is the friction factor expressed as:

$$C_f = 0.0592 \, \mathrm{Re}_x^{-0.2} \tag{37}$$

Re_x is the Reynolds number based upon the distance x from the leading edge and is valid for values > 1.10 x 10^7 [15]:

$$\mathrm{Re}_x = G \frac{x_e}{\mu_g} \tag{38}$$

where G is the free stream gas flow ($\rho_g U_g$). In order to take into account growing boundary layer present in the flow, x is replaced by:

$$x_e = 3.53D \left[1 + \left(\frac{x}{3.53D} \right)^{-1.2} \right]^{-1/1.2} \tag{39}$$

The convective coefficient is dependant on the Reynolds number (mass velocity). Table 1 shows how it varies at a distance of 15 cm (~ half the reflector distance) from the liquid injector point using Equations 34 through 39 with hydrogen as a coolant. The Reynolds numbers are provided up to 10^7, which is the upper experimental limit for which the equations have been verified.

Table 1. Convective Transfer Coefficient Variation with Reynolds Number

Reynolds Number	Heat Transfer Coefficient
1.00E+05	0.05
2.50E+05	0.10
5.00E+05	0.17
7.50E+05	0.24
1.00E+06	0.30
2.50E+06	0.63
5.00E+06	1.10
7.50E+06	1.52
1.00E+07	1.91

From these values of the heat transfer coefficient, we can see that the lower the Reynolds number, the lower the convective heat flux will be. If the incoming radiation is on the order of 10^6 K, then from Equation 33:

$$\dot{Q}_{conv} \sim 10^5 \text{ W/cm}^2 \tag{40}$$

This produces a liquid evaporation rate (per area) of:

$$\dot{m}_v = \frac{\dot{Q}_{tot}}{\lambda} \sim 30 \text{ kg}/\text{s cm}^2 \tag{41}$$

We can thus see the engineering difficulties encountered with a cooling system designed for such a significant incoming flux; this is a significant mass flow rate for such a small area. The liquid film thickness and average velocity can be estimated using the laminar "Couette flow" result:

$$\delta = \sqrt{\frac{2\mu\Gamma}{\rho\tau_w}} \ , \tag{42}$$

where τ_ω is the wall shear stress and can be calculated from:

$$\tau_w = \tfrac{1}{2} C_f G(U_g - U_l)\,, \tag{43}$$

and the liquid velocity can be found from:

$$U_{liq} = \frac{\Gamma}{\rho\delta} \tag{44}$$

4.2.2 Heat Transfer

In order to estimate the film cooling length, the heat transfer relations derived by Stechman [19] will be utilized. Stechman predicted the heat transfer coefficient from the combustion gas to the film coolant and from the film coolant to the wall by modifying the one-dimensional Bartz equation to take into account the effect of the liquid and gaseous film. Equation (45) calculates the heat transfer coefficient from the film coolant to the wall:

$$h_g = \left(\frac{0.026\mu_l^{0.2}}{D^{0.2}\,\mathrm{Pr}_l^{0.667}}\right)\left(\frac{\dot{m}_l}{A}\right)^{0.8}\left(\frac{H_r - H_w}{T_r - T_w}\right)\xi \tag{45}$$

where μ_l is the liquid dynamic viscosity, D is the reflector diameter, Pr is the Prandtl number, A is the reflector area, H_r and H_w are the recovery and wall enthalpy, T_r and T_w are the recovery and wall temperature, and ξ is a parameter which accounts for the static property change as given by:

$$\xi = \left(\frac{T^{0.8}}{T_g^{1.2}T_l^{0.667}}\right) \tag{46}$$

The heat transfer coefficient for the liquid is given by:

$$h_l = 0.0288\left(\frac{Cp_l}{\mathrm{Pr}_l^{0.667}\ \mu_l x^{0.2}}\right)\left(\frac{\Omega\dot{m}u_l h_g\,\mathrm{Pr}_l\ \rho_l}{\pi(D/2)Cp_g}\right)^{0.4}, \tag{47}$$

where Cp_l is the liquid heat capacity, and x is the axial distance. The film cooling length was also estimated by Stechman, as shown in Equation 48. It can be seen from this equation that the length is proportional to the heat capacity and the heat of vaporization:

$$L_c = \frac{\Omega \dot{m}_l \, Cp_l (T_{sat} - T_i)}{Ph_g (T_r - T_{sat})} + \frac{\Omega \dot{m}_l \, H_v}{Ph_g (T_r - T_{sat})}, \tag{48}$$

where Ω is an empirical correction factor with a value between 0.5 – 1, P is the chamber perimeter, T_{sat} is the saturation temperature, and H_v is the total enthalpy of the vapor. The first term on the right represents the distance from the injection point for which the effective gas temperature varies from its initial injection temperature to its saturated liquid temperature, and the second term represents the length which is required for the hot gas to completely vaporize the film. Using the appropriate values for the parameters evaluated in Equation (48), a film cooling length of 3.2 cm is calculated, assuming a liquid mass flow rate of 15 kg/s.

4.3 Regenerative Cooling

Regenerative cooling is the process where a coolant is passed through a channel adjacent to a wall to lower the wall temperature. The steady state heat transfer through the chamber wall of a liquid-cooled rocket chamber can be treated as a series type, steady-state heat transfer problem with a large temperature gradient across the gaseous film on the inside of the chamber wall, a temperature drop across the wall, and a third temperature drop across the film of the moving cooling fluid. It is a combination of convection at the boundaries of the flowing fluids and conduction through the chamber walls. The general steady-state heat transfer equations for regeneratively cooled thrust chambers can be expressed as [20]:

$$\begin{aligned} q &= h(T_o - T_l) = Q / A \\ &= \frac{T_g - T_l}{1/h_g + t_w/\kappa + 1/h_l} \\ &= h_g (T_o - T_{wg}) \\ &= (\kappa / t_w)(T_{wg} - T_{wl}) \\ &= h_l (T_{wl} - T_l) \end{aligned} \quad , \tag{49}$$

where q is the heat transferred per unit area per unit time, T_g the absolute chamber gas temperature, T_l the absolute coolant liquid temperature, T_{wl} the absolute wall temperature on the liquid side of the wall, T_{wg} the absolute wall temperature on the gas side of the wall, h the overall film coefficient, t_w the thickness of the chamber wall, and κ the conductivity of the wall material. An illustration of these parameters is shown in a qualitative temperature profile diagram in Figure 14 [20].

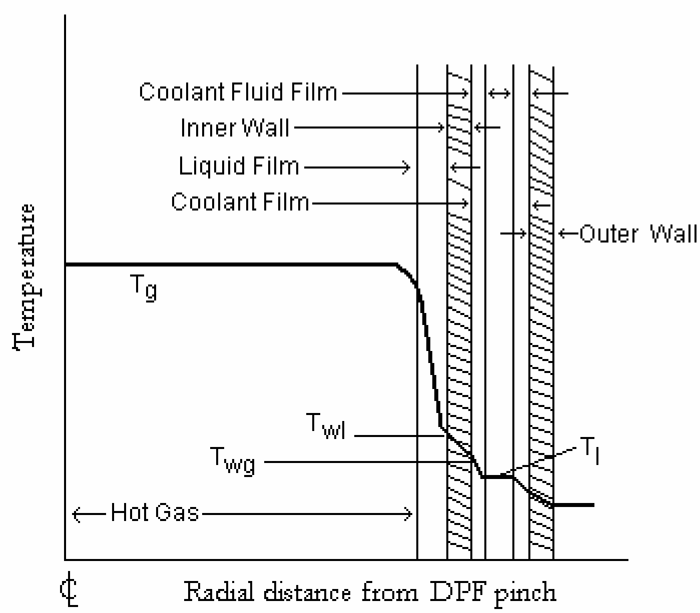

Figure 14: Qualitative Temperature Profile of Radiation Reflector

The film coefficients can be calculated through the use of Equations 45 and 47. The important quantities for controlling the heat transfer across a rocket chamber wall are the fluid film boundaries established by the combustion products on one side of the wall and the coolant flow on the other. The gas film coefficient largely determines the numerical value of the heat transfer rate, and the liquid film largely determines the value of the wall temperatures. The necessary regenerative cooling is heavily dependant on the amount of heat the liquid film on the surface is able to take away.

4.4 Limitations of Cooling Models

The major limitation to the liquid cooling models developed and used is that there is no theory or experimental work done in our area of interest; chemical rocket chamber conditions are vastly different from fusion chamber conditions. It is therefore unclear how relevant the equations presented are. Additionally, the convective transfer equations are all derived with the assumption that radiation is negligible, which very well might prove to be the complete opposite. However, the analysis presented may provide order of magnitude estimates for the cooling requirements, in which case it can be seen that a very high injection speed and mass flow rate (30 kg $s^{-1}cm^{-2}$) will be necessary to counteract the extremely high temperatures found near the wall regions.

5.0 CONCLUSIONS

For a 500 kN, 2000 Isp dense plasma focus propulsion device, the energy and power are 1.23×10^5 J/cm^2 and 1.26×10^6 W/cm^2. The flux to the wall depends on the exposed area of the reflector, although it has been shown that it would be advantageous to have a small reflector. This is because the reemission increases with flux in the case of a gold film reflector; and in the case of multilayers, maximum reflectivity occurs at small angles. Additionally, a small reflector would greatly decrease cooling needs. The use of gold film, Hohlraum-like cavities has been explored; and for an incident flux of 10^{12} W/cm^2, the radiation will be reemitted approximately 10 times before being lost, according to the numerical work done by Murakami. In the case of multilayer structures, x-ray energies of DPF have not yet been investigated, although the trend is moving in that direction. Despite the advantages of multilayer structures over single element layers, such as a greater energy band of reflectance, multilayer structures would not be able to handle the incoming energy flux levels characteristic of the p-^{11}B pinch; and it is unclear whether low Z materials or cooling methods could aid. This is due in part to the lack of theory and experiment in cooling methods in DPF-like environments. A 50% reflection rate was assumed in the prior DPF study, which seems out of reach of current multilayer capabilities, but within the reach of single-film Hohlraum cavities. An investigation of inverse-Bremsstrahlung is necessary; if there are 10 passes of photons before being lost, it is very possible that the radiation will be reabsorbed in the pinch region.

6.0 REFERENCES

[1] Thomas, R., et.al., "Advancements in Dense Plasma Focus (DPF) for Space Propulsion," *Space Technology & Applications International Forum (STAIF) Conf. Proc*. **746**, 536, 2005. DTIC AD #ADA433824.

[2] Glasstone, S., and Lovberg, R.H., **Controlled Thermonuclear Reactions**, New York: John Wiley & Sons, 1985.

[3] Huddlestone, R.H., Leonard, S.L., **Plasma Diagnostic Techniques**, New York: Academic Press, 1965.

[4] Kammash, T., **Fusion Reactor Physics: Principles and Technology**, Ann Arbor Science, 1975.

[5] Nishimura, H., et. al., "X-ray Confinement in a Gold Cavity Heated by a 351 nm Laser Light," *Phys. Rev. A.*, **44**, pg. 8323, Dec. 1991.

[6] Haan, S., "On Target Designing for Ignition," accessed 15 Aug 2005, available from the internet at http://www.llnl.gov/str/Haan.html.

[7] Pakula, R., and Sigel, R., "Self Similar Expansion of Dense Matter Due to Heat Transfer by Nonlinear Conduction," *Phys. Fluids*, **28**, pg. 232, 1985.

[8] Murakami, M., Meyer-Ter-Vehn, J., "Indirectly Driven Targets for Inertial Confinement Fusion," *Nuc. Fusion*, **31**, pg. 1315, 1991. .

[9] Tsakiris, G.D., and Eidmann, K., "An Approximate Method for Calculating Plank and Rosseland Mean Opacities in Hot, Dense Plasmas," *J. Quant. Spectroc. Radiat. Transfer*, **38**, pg. 353, 1987.

[10] Joensen, K.D., "Broad-band Hard X-Ray Reflectors," *Nuc. Instr. and Methods in Phys. Research B*, **132**, pg. 221, 1997.

[11] Windt, D.L., "Optical Constants for Hard X-Ray Multilayers Over the Energy Range E = 35 -180 keV," *Proc. SPIE*, **5168**, pg 35.

[12] Rehm, C., Agamalian, M., Klose, F., "Neutron Supermirrors: Design and Application," Oak Ridge National Laboratory Report, accessed 15 Aug 2005, available from the internet at: www.sns.gov/Users/instrument_systems/pdfs/optical/new/OCT-Report NeutronSupermirrors.pdf.

[13] Kim, D., et. al., "Characterization of a Multilayer Soft X-Ray Reflector Fabricated by Pulsed Laser Deposition," *Applied Surface Science*, **127**, pg. 531, 1998.

[14] Coulbert, C.D., “Selecting Cooling Techniques for Liquid Rockets for Spacecraft,” AIAA – 1963 – 241, 1963.

[15] Yu, Y.C., Schuff, R.Z., Anderson, W.E., “Liquid Film Cooling Using Swirl in Rocket Combusters,” AIAA – 2004 – 3360, 2004.

[16] Gater, R.A., L’Ecuyer, M.R., “A Fundamental Investigation of the Phenomena that Characterize Liquid Film Cooling,” Jet Propulsion Center, Purdue University, NASA TM-69-1, 1969.

[17] Grissom, W.M., “Liquid Film Cooling in Rocket Engines,” AEDC – TR – 91 -1, 1987. DTIC AD# ADA234288.

[18] Monde, M., and Katto, Y., “Burnout in a High Heat Flux Boiling System with an Impinging Jet,” *Int. Journ. Of Heat and Mass Transfer*, **21**, pg. 295, 1978.

[19] Stechman, R.C., Oberstone, J., Howell, J.C., “Design Criteria for Film Cooling for Small Liquid Propellant Rocket Engines,” AIAA – 1968 – 617, 1968.

[20] Sutton, G., Biblarz, O., **Rocket Propulsion Elements**, Wiley – Interscience, 2000.

AFRL-PR-ED-TR-2005-0068
Primary Distribution of this Report:

AFRL/PRSP (15 CD)
Dr. Frank Mead
10 E. Saturn Blvd
Edwards AFB CA 93524-7680

AFRL/PRSA (1 CD)
Dr. Jean-Luc Cambier
10 E. Saturn Blvd.
Edwards AFB CA 93524-7680

AFRL/PR (1 CD)
Dr. Alan Garscadden
1950 Fifth Street
Building 18
Wright-Patterson AFB, OH 45433-7251

AFRL/PR Technical Library (2 CD + 1 HC)
6 Draco Drive
Edwards AFB CA 93524-7130

Chemical Propulsion Information Agency (1 CD)
Attn: Tech Lib (Dottie Becker)
10630 Little Patuxent Parkway, Suite 202
Columbia MD 21044-3200

Dr. Robert Sierakowski (1 CD)
AFRL/MN
101 W. Eglin Blvd., Ste 105
Eglin AFB FL 32542

Dr. Eric Davis (10 CD)
IASA
4030 Braker Ln. W., Suite 300
Austin TX 78759

Dr. Dana Andrews (1 CD)
Andrews Space & Technology
525 S. Douglas, Suite 210
El Segundo CA 90245

Dr. Jim Degnan (1 CD)
AFRL/DEHP
Kirtland AFB, NM 87117

Dr. Greg Benford (1 CD)
Physics Department
University of California
Irvine, CA 92717

Dr. Jim Benford (1 CD)
Microwave Sciences, Inc.
1041 Los Arabis Ln.
Lafayette, CA 94549

Dr. Gary L. Bennett (1 CD)
7517 West Devonwood Dr.
Boise, ID 83703

Dr. Mitat Birkan (1 CD)
AFOSR/NA
801 N. Randolf St.
Arlington, VA 22203

Dr. Jon Campbell (1 CD)
P.O. Box 295
Harvest, AL 35749

Mr. Buzz Aldrin (1 CD)
233 Emerald Bay
Laguna Beach CA 92651

Dr. Phil Carpenter (1 CD)
US Dept. of Energy
Oak Ridge National Laboratory
P.O. Box 2008, MS: 6269
Oak Ridge, TN 37831

Dr. Brice N. Cassenti (1 CD)
Pratt & Whitney Aircraft
400 Main Street – MS: 163-07
East Hartford, CT 06108

Dr. Chan K. Choi (1 CD)
Purdue University
School of Nuclear Engineering
West Lafayette, IN 47907

Dr. Terry Kammash (1 CD)
University of Michigan
Nuclear Engineering Dept.
Ann Arbor, MI 48109

Dr. David Azavedo (1 CD)
United Technology/Pratt & Whitney
57 Barnwood Rd.
Manchester CT 06040

Dr. Robert Frisbee (1 CD)
JPL, MS 125-109
4800 Oak Grove Dr.
Pasadena, CA 91109

Dave Froning (1 CD)
Flight Unlimited
P.O. Box 180
Gumeracha SA 5233
Australia

George D. Hathaway (1 CD)
Hathaway Consulting Services
39 Kendal Ave.
Toronto, Canada, Ontario
Canada M5R 1L5

Clark W. Hawk, Director (1 CD)
Propulsion Research Center
University of Alabama in Huntsville
5000 Technology Drive, TH S-266
Huntsville, AL 35899

Alan C. Holt (1 CD)
NASA/Johnson Space Center
Code OD
Houston, TX 77058

Dr. Steven Howe (1 CD)
19 Karen Lane
Los Alamos, NM 87544

Mike Kaiserman (1 CD)
Raytheon Missile Systems Company
Bldg 805, M/S C3
Tucson, AZ 85734

Dr. George Miley (1 CD)
University of Illinois, Dept. of Nuclear Engr.
214 Nuclear Engineering Laboratory
103 South Goodwin Ave.
Urbana, IL 61801

Marc Millis (1 CD)
NASA Glenn Research Center
M.S. SPTD-2
21000 Brookpark Road, MS: 86-2
Cleveland, OH 44135

Dr. Jordon Kare (1 CD)
222 Canyon Lakes Pl.
San Ramon, CA 94583

Ron J. Kita (1 CD)
87 Shady Springs DR.
Doyelstown, PA 18901

Dr. Gerald L. Kulcinski (1 CD)
Nuclear Engineering Dept.
University of Wisconsin
1500 Johnson Dr.
Madison, WI 53706

Dr. Geoffrey A. Landis (1 CD)
Sverdrup Technology
21000 Brookpark Rd., MS 302-1
Cleveland, OH 44135

Dr. Michael LaPointe (1 CD)
Marshall Space Flight Center
MSFC AL 35812

Dr. Sheldon Meth (1 CD)
DARPA
Tactical Technology Office
3701 N. Fairfax Dr.
Arlington, VA 22203

Dr. Michael M. Micci (1 CD)
Prof. of Aerospace Engineering
233 E. Hammond Bldg.
University Park, PA 16802

Dr. Hal Puthoff (1 CD)
Institute for Advanced Studies
4030 Braker Lane, West
Suite 300
Austin, TX 78759

Dr. Eric E. Rice (1 CD)
Orbital Technologies Corp.
402 Gammon Place, Suite 10
Madison, WI 53719

Ranney Adams (1 CD + 1 HC)
AFRL/PROI
2 Draco Drive
Edwards AFB, CA

Dr. Aurthur Morrish (1 CD)
DARPA/ATO
3701 N. Fairfax Dr.
Arlington, VA 22203

Dr. Paul Murad (1 CD)
Sr. Analyst, Director for Intel Production
Missile & Space Intel Center
Defense Intelligence Agency
Washington, DC 20340-6054

Dr. Brian Palaszewski (1 CD)
NASA Glenn Research Center
21000 Brookpartk Road, MS: 5-10
Cleveland, OH 44135

Dr. Alan Pike (1 CD)
DSAS
1988 Crescent Park Drive
Reston, VA 20190

Dr. Dennis Pelaccio (1 CD)
SAIC
8100 Shaffer Parkway, Suite 100
Littleton, CO 80127

Ben Plenge (1 CD)
101 W. Eglin Blvd
Suite 342
Eglin AFB, FL 32542-6810

Dr. James Powell (1 CD)
Plus Ultra Technologies, Inc.
25 East Loop Rd.
Stony Brook, NY 11970-3350

Mr. Charles A. Yost (1 CD)
Electric Spacecraft Journal
73 Sunlight Drive
Leicester, NC 28748

Dr. John Brandenburg (1 CD)
6272-B Rosehill Ct.
Alexandria VA 22310

Dr. Dennis Keefer (1 CD)
The University of Tennessee Space Institute
Tullahoma TN 37388

Dr. George Schmidt (1 CD)
NASA HQ
300 E. Street SW
Washington, DC 20546

Steve Squires (1 CD)
Directorate of Applied Technology
Test and Simulation
STEWS-DATTS-OO
WSMR, NM 88002

Robert Talley (1 CD)
Topaz 2000, Inc
3380 Sheridan Dr.
Suite 172
Amherst, NY 14226

Dr. Kenneth D. Ware (1 CD)
Defense Nuclear Agency
Simulation Technology
6801 Telegraph Road
Alexandria, VA 22310

Dr. Feiedwardt Winterberg (1 CD)
University of Nevada
Desert Research Institute
Reno, NV 89507

Dr. Young Bae (1 CD)
1101 Bryan Ave.
Suite C
Tustin, CA 92780

Dr. Thomas M York (1 CD)
1215 Inverary Pl.
State College, PA 16801

Dr. Robert J. Barker (1CD)
AFOSR/NE
801 N. Randolf St.
Arlington, VA 22203

Mr. Bill Haloulakos (1 CD)
1031 E, Fairmont Rd.
Burbank CA 91501

Dr. David Q. King (1 CD)
Aerojet
P.O. Box 97009
Redmond WA 98073

Dr. Eric J. Lerner (1 CD)
Lawrenceville Plasma Physics
20 Pine Knoll Dr.
Lawrenceville NJ 08648

Dr. Patrick McDaniels (1 CD)
Sandia National Laboratories
MS 1133, P.O. Box 5800
Albuquerque NM 87185

Mr. Yoshinari Minami (1 CD)
NEC Patent Service, Morinaga Plaza Bldg.
18F,33-1, Shiba 5-Chome,
Minato-Ku , Tokyo 108-8425
Japan

Dr. Kenneth G. Moses (1 CD)
Fusion Physics
3547 Voyager St., Suite 104
Torrance CA 90503

Dr. Reece Roth (1 CD)
University of Tennessee
Dept. of Electrical Engineering
316 Ferris Hall
Knoxville TN 37996

Dr. Paul Czysz (1 CD)
HyperTech Concepts
142 Laduemont Dr.
St. Louis MO 63141

Maj Peter A. Garretson (1 CD)
HQ USAF/XPXC 5C169
1070 Air Force Pentagon
Washington DC 20330

Dr. Takashi Nakamura (1 CD)
PSI 2110 Omega Rd., Suite D
San Ramon CA 94583

Dr. Leo Christodoulou (1 CD)
DARPA/DSO
3701 N. Fairfax Dr.
Arlington VA 22203

Mr. Greg V. Meholic (1 CD)
The Aerospace Corp.
P.O. Box 92957 – M4/970
Los Angeles CA 90009

Dr. Jordan G. Maclay (1 CD)
Quantum Fields
20876 Wildflower Ln.
Richland Center WI 53581

LtC Timothy Lawrence (1 CD)
Hd. Qtrs. USAFA
Dept. of Astronautics, Suite 1M 147
2354 Fairchild Dr.
USAFA CO 80840

Mr. Kimo Nishino (1 CD)
Toyota Motor Corp.
23-22 IZUMI, 1 CHOME
HIGASHI-KU, NAGOYA 461-8711
Japan

Dr. Claude Phipps (1 CD)
200A Ojo de la Vaca Rd.
Santa Fe NM 87505

Dr. John Rusek (1 CD)
School of Aero & Astro Engineering
Purdue University
1282 Grissom Hall
West Lafayette IN 47907

Dr. Shigeaki Uchida (1 CD)
Institute for Laser Technology
2-6 Yamadaoka SUITA
OSAKA 565-0871
Japan

Dr. Martin Tajmar (1 CD)
ARC Seibersdorf Research GmbH
A2444 Seibersdorf
Austria

Dr. Rodney Burton (1 CD)
101 Transportation Bldg.
104 S. Mathews Ave.
Urbana IL 61801

Dr. William Goodman (1 CD)
Schafer Corp.
2309 Renard Pl SE, Suite 300
Albuquerque NM 87106

Dr. Donald G. Messitt (1 CD)
Aerojet
P.O. Box 13222
Sacremento CA 95813

Robert Thomas (1 CD)
Fusion Studies Laboratory
University of Illinois at Urbana-Champaign
103 South Goodwin Avenue
Urbana IL 61801

Sean D. Knecht (1 CD)
4746 11th Ave. NE, Apt. 309
Seattle, WA 98105

Defense Technical Information Center
(1 Electronic Submission via STINT)
Attn: DTIC-ACQS (Pat Mawby)
8725 John J. Kingman Road, Suite 94
Ft. Belvoir VA 22060-6218